

# Photopolymerized Patterning and Materials to Enhance Neural Prosthetic Performance

By Bradley W. Tuft, Linjing Xu, Austin Hangartner, Scott White, Marlan Hansen and Allan Guymon

*This article was awarded "Best Paper" at the 2014 RadTech Technology Expo and Conference.*

Performance of successful neural prosthetics, such as the cochlear implant (CI), has not significantly improved in recent years due to poor spatial resolution at the nerve-implant interface. Directing neurites toward target electrodes may reduce problematic signal spread and improve stimulatory specificity. Consequently, our work utilizes the spatial and temporal control inherent to photopolymerization methodology to fabricate micropatterned methacrylate polymers that direct nerve cell growth based on substrate topographic and stiffness cues. Micropatterned substrates are formed in a rapid, single-step reaction by selectively blocking initiating light with glass-chrome photomasks that have repeating line-space features with a pitch of 10-100  $\mu\text{m}$  in width. The resultant pattern is a continuous

series of ridges and grooves at regular intervals that can be used for cellular contact guidance studies. Microfeature depth is controlled and reproducibly generated from  $220\pm 40$  nm to  $16\pm 1.3$   $\mu\text{m}$  by shuttering the light source at different time steps during the reaction and by modulating photoinitiator concentration. The ultimate goal of the research is to develop materials that predictably orient regenerative nerve cell growth and improve neural prosthetic stimulatory specificity and thus improve patient outcomes.

## Introduction

Neural prostheses electrically stimulate neural tissue to restore or augment remaining motor and sensory functions of neural pathways that were lost or damaged due to disease or physical trauma. However, commercially available prostheses such as the cochlear implant and promising developmental prostheses such as the retinal implant suffer from poor spatial signal resolution which limits their ultimate performance.<sup>1-3</sup> For example, retinal prosthesis simulation is limited to few sensory pixels due, in part, to electrical signal overlap among target neurons in the retina caused by spatial separation of stimulating electrodes from the neural tissue.<sup>3</sup> The CI enables basic speech perception,

## FIGURE 1

### Representation of the cochlear implant (CI)

The CI provides auditory perception to individuals with severe hearing loss and is currently the most successful neural prosthetic.

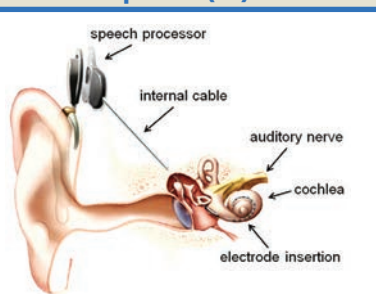
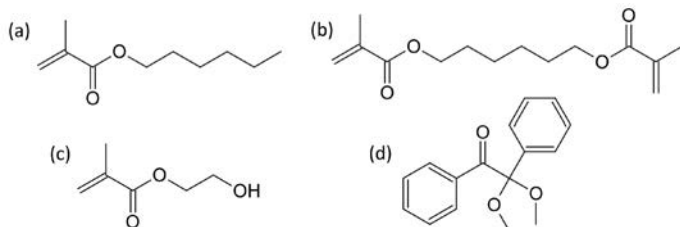


## FIGURE 2

### Chemical structures of monomers and photoinitiator used in methacrylate micropattern fabrication

Shown are (a) hexyl methacrylate (HMA), (b) 1,6-hexanediol dimethacrylate (HDDMA), (c) hydroxy ethyl methacrylate (HEMA), and (d) 2,2-dimethoxy-2-phenylacetophenone (DMPA).



but suffers from comparable spatial signaling limitations due to nonspecific excitation of neurons within the cochlea which preclude high-fidelity tonal simulation for the user (Figure 1). Subsequently, CI patients struggle with complex auditory stimuli such as voice comprehension in noisy environments and music appreciation.<sup>4,5</sup>

Driving regenerative neural processes into closer spatial proximity of specific stimulating electrodes would allow for lower current trigger thresholds that would reduce problematic signal overlap, enable higher stimulatory specificity and perhaps lead to greater precision in both signal input and biological functional output.<sup>2,6-11</sup> However, for the proximate growth strategy to be effective, the tone-dependent spatial arrangement of nerves must be preserved and will require directional control of regenerating neurites.<sup>1</sup> Moreover, since the nervous system depends on location-specific signaling, similar spatial resolution limitations are anticipated for any device that interfaces with the nervous system. Consequently, precise spatial neural regeneration will be crucial to realize the functional potential of next-generation neural prostheses.

Therefore, as a step toward enhanced neural prostheses performance, we are exploring the use of photopolymerization to fabricate micropatterns on biocompatible methacrylate polymers to support and guide neurite regeneration. Photopolymerization is a rapidly expanding biomaterials production platform due to its mild reaction conditions, high reaction rates at room temperature and chemical versatility of monomer systems. The overall objective of the research is to translate fundamental photopolymerization methodology and understanding of nerve cell material interactions into directed nerve regeneration that improves the ultimate performance of neural prosthetics.

### Experimental

#### Glass Substrate Methacrylation

Standard glass microscope slides were functionalized with a silane coupling agent to prevent delamination of the polymer from the glass during sample characterization and cellular studies. Prior to treatment with the coupling agent, slides were first cleaned and oxidized with O<sub>2</sub> plasma for three minutes at 30 W RF power (PDC-001 Harrick Plasma Expanded Cleaner, Ithaca, N.Y.) while under 300 mTorr

vacuum. Immediately following removal from the plasma chamber, the slides were immersed in a 1/100 v/v solution of 3-(trimethoxysilyl)propyl methacrylate (Aldrich) and n-hexane (Aldrich) and were left overnight in a covered container at room temperature (~21°C). Each slide was then rinsed with fresh hexanes and allowed to dry in a fume hood before being placed in a sealed container. Functionalized slides were immediately used for polymerization when removed.

#### Photopolymerization of Micropatterned Methacrylate Thin Films

Monomer mixtures of hexyl methacrylate (HMA, Aldrich), 1,6-hexanediol dimethacrylate (HDDMA, Aldrich) and hydroxy ethyl methacrylate (HEMA, Aldrich) were prepared with 1 wt% of 2,2-dimethoxy-2-phenylacetophenone (DMPA, BASF) as the photoinitiator (Figure 2). Copolymer compositions are represented as whole numbers (e.g., 40/60, 50/50), but each polymer fraction takes into account the 1 wt% for the photoinitiator. A volume of 20 µL from pre-polymer formulations was pipetted onto the center of a functionalized slide then covered with a 2.54 cm x 2.54 cm x 0.1 cm glass chrome Ronchi rule photomask (Applied Image Inc., Rochester, N.Y.) for parallel patterns or with a cut, untreated glass slide of the same dimensions for unpatterned samples.

Formulations were spread evenly between the substrate and photomask. Photopolymerization was carried out with a high-pressure, mercury-vapor arc lamp (Omnicure S1500, Lumen Dynamics, Ontario, Canada) at a 365 nm light intensity of 16 mW/cm<sup>2</sup>. Light intensity was measured with a Cole-Parmer Series 9811 radiometer. The curing module was equipped with an 8 mm aperture x 50 mm length beam homogenizing fused silica light pipe

(Edmund Optics) and a collimating lens (RLQ-1, Asahi Spectra). Microfeature amplitude was tuned by shuttering UV radiation at specific times to prevent further initiation events resulting in rapid termination of the polymerization. Following the set exposure time, the photomask was removed from the polymer and the sample was washed with 95% ethanol to remove residual surface monomer.

### White Light Interferometry

Micropattern feature spacing and depth were measured by white light interferometry (Dektak Wyko 1100 Optical Profiling System, Veeco). Feature amplitude was measured as the difference between a maximum ridge value and an adjacent minimum groove value. For each composition and exposure time, average feature height was determined by measuring channel amplitude in nine different areas across the surface ( $n \geq 3$ ). Feature spacing or periodicity was measured as the distance between the highest points on adjacent ridges and was consistent with photomask band spacing. Measurements and 3D images were generated using *Vision* software.

### Scanning Electron Microscopy

Micropattern morphology of each composition was further characterized

by scanning electron microscopy (SEM) (S-4800, Hitachi). Conductive silver paint was applied to the bottom of glass substrates modified with micropatterned methacrylate thin films for mounting on aluminum SEM stubs to acquire top-down images. For cross-sectional images, a glass etcher was used to etch the sample on the side opposite of the thin polymer film; and patterned polymers were then fractured and mounted vertically on specimen stages. The SEM specimen stage was angled using automated stage and software controls. Each polymer surface was sputter coated with gold prior to examination by SEM. Electron accelerating voltage was set at 2 kV.

### Photo-Differential Scanning Calorimetry (Photo-DSC)

Kinetic measurements were made during the photopolymerization using differential scanning calorimetry (Perkin-Elmer, DSC). A 3 mg mixture of each methacrylate composition was deposited into a dimpled aluminum pan and photopolymerized at 30°C under the same lamp and light intensity as used for micropattern fabrication. A reference aluminum pan was placed in the reference holder of the instrument (Perkin-Elmer DSC). Light intensity of the high-pressure,

mercury-vapor arc lamp was tuned using shutter opening controls on the module. Maximum polymerization rate was calculated at the point of highest heat flow and double-bond conversion was determined by integrating the polymerization rate profile. Design Expert 9 was used for design of experiment (DOE) modeling and analysis of kinetic data.

### Spiral Ganglion (SG) Neuron Cell Culture

Dissociated SG cultures from 3- to 5-day-old rat pups were prepared and plated as previously described.<sup>12,13</sup>

### Quantification of Neurite Alignment

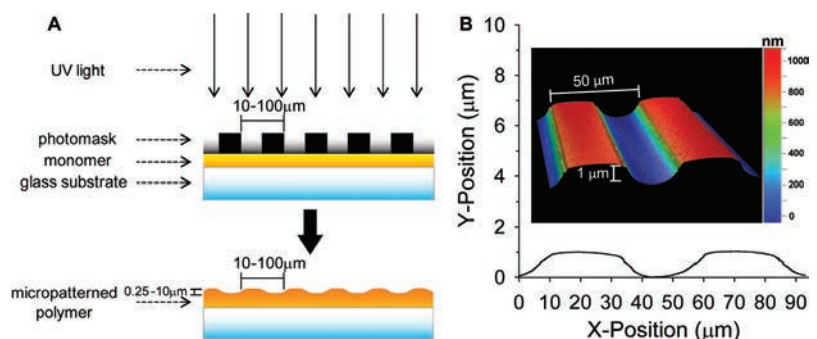
Total neurite length ( $T_L$ ) was measured in Image J as previously described.<sup>13</sup> Aligned length ( $A_L$ ), distance traveled only in the direction of the line-space grating, was similarly measured in Image J. Neurite alignment was subsequently calculated as a ratio of aligned length to total neurite length ( $A_L/T_L$ ). Neurites that are strongly guided by the pattern have alignment ratios approaching one. Conversely, neurites that wander—or do not strongly track microfeatures—have much lower ratios. Neurites with alignment ratios close to one-track micropattern feature direction throughout the majority of their length.

## FIGURE 3

### Photopatterning process schematic

(A) Photoinitiator and monomer systems are selectively exposed to UV light through a photomask resulting in raised microfeatures across the surface.

(B) 2D Profile of micropatterned HMA-co-HDDMA with a periodicity of 50  $\mu\text{m}$  and an amplitude of 1  $\mu\text{m}$ . Inset: 3D representation of a 100  $\mu\text{m}^2$  area derived by white light interferometry.



## Results and Discussion

### Photopolymerization of Micropatterns

Microfeatures are generated across polymer surfaces by means of the spatial control of photopolymerization. Prepolymer reaction mixtures are selectively exposed to UV irradiation through photomasks that have band spacing at size scales that are relevant to the cell (Figure 3). Photomasks for parallel line-space gratings consist of alternating reflective (chrome) and transparent (glass) bands. During UV exposure, polymerization occurs rapidly under transparent bands that transmit full, incident light intensity from the source which results in

raised ridges. Light that is diffracted after passing through the microscale transparent bands and the migration of reactive chains during the reaction cause slow polymerization in areas under the reflective bands which results in surface depressions between raised features. As a result, a pattern of parallel microridges and grooves of uniform width and amplitude rapidly develop across the substrate surface in a single fabrication step.

### Tunable Surface Features

Surface features are readily tuned by altering simple parameters of the photopolymerization. Namely, control over feature height is achieved by

changing reaction parameters such as initiator concentration and species, light intensity and UV exposure time (Figures 4-5). For example, maximum feature amplitude was increased by 50% from 8  $\mu\text{m}$  to 12  $\mu\text{m}$  at low DMPA concentrations (data not shown). However, micropatterns cured with bis(2,4,6-trimethylbenzoyl) phenylphosphine oxide (BAPO) as the photoinitiator showed the opposite trend with high maximum amplitudes being captured with higher initiator content. For the HMA-co-HDDMA system, absolute feature height is tuned by approximately two orders of magnitude  $\sim 100\text{ nm}$ -10  $\mu\text{m}$  (results are only shown for 1-10  $\mu\text{m}$  regime).

Increases in light intensity raised reaction rates and shifted final amplitude profiles to earlier time steps and also decreased the maximum attainable amplitude for microfeatures which was likely due to decreases in diffusion of reactive species caused by faster polymerization rates (Table 1). Feature spacing is controlled based on pattern dimensions in the photomask. However, the maximum feature height that could be attained for a given photoinitiator concentration and light intensity is limited by diffraction of light as it passes through photomask bands and by diffusion of reactive species that migrate more readily into shadowed areas as band space decreases (Table 2).

### Micropattern Characterization by SEM

In addition to characterization by white light interferometry, SEM was used to confirm microfeature dimensions and homogeneity (Figure 5). 3D angled side views demonstrate that parallel ridges and grooves extend across the substrate surface and that the features are homogenous, excluding edge effects. The smooth transitions between

TABLE 1

### Modulation of light intensity modifies micropattern formation

365 nm Light Intensity (mW/cm <sup>2</sup> )	Max Amplitude ( $\mu\text{m}$ )	$t_{\text{max}}$ (s)
8	8.09 $\pm$ 0.55	90
15	8.24 $\pm$ 0.69	79
19	7.91 $\pm$ 0.40	75
24	7.86 $\pm$ 0.25	71
55	7.27 $\pm$ 0.25	64
80	6.71 $\pm$ 0.23	58

Increasing light intensity tightens the channel amplitude versus exposure time profile and shifts it to lower time steps.

TABLE 2

### Photomask band spacing significantly impacts micropattern amplitude

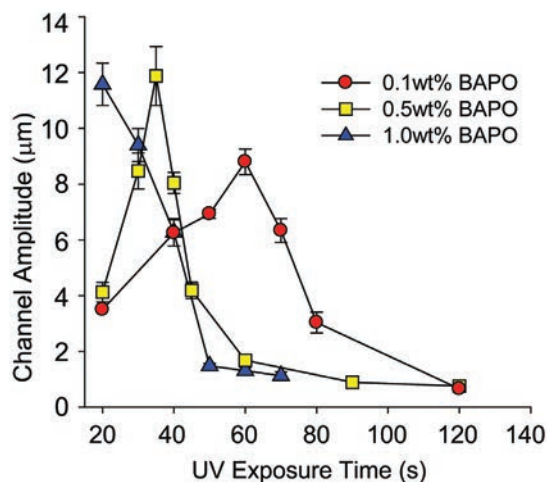
Mask Periodicity ( $\mu\text{m}$ )	Max Amplitude ( $\mu\text{m}$ )	$t_{\text{max}}$ (s)
10	1.81 $\pm$ 0.07	76
33	5.72 $\pm$ 0.36	76
50	8.21 $\pm$ 0.65	76
100	10.75 $\pm$ 1.09	76

Diffraction of light and diffusion of reactive species limit the maximum amplitude that can be obtained under given reaction conditions.

## FIGURE 4

### Micropattern feature height is tuned by modulating photoinitiator concentration and species and by varying UV exposure time

Increasing BAPO photoinitiator concentration shifted amplitude profiles to smaller time steps and increased maximum attainable amplitude by 50%. Photomask band spacing was 25  $\mu\text{m}$  and a 16mW/cm<sup>2</sup> light intensity at 365 nm was used.



microfeatures on the substrate surface are distinctly different from sharp features generated by etch or imprint lithography.

Studying nerve or general cell contact guidance on gradually sloping features remains largely unexplored and may provide additional insight into cellular mechanisms that provide a causal response to surface features. Additionally, sloping features enable delicate biochemical studies that probe the effects of pharmacological agents on neurite guidance that may otherwise be difficult to explore with the potentially masking effects of sharp or “infinite” slope features.

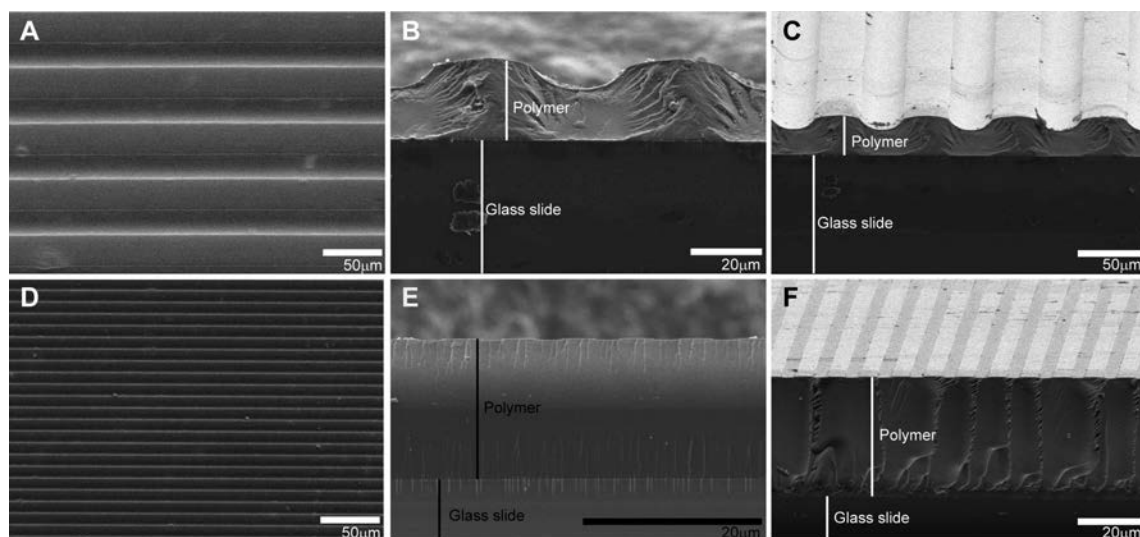
### Kinetics of Methacrylate Photopolymerization

A tricomponent mixture design of experiments (DOE) was used to model and predict basic reaction kinetics of methacrylate monomer mixtures relevant to neuronal contact guidance studies. Response surface models were

## FIGURE 5

### Representative SEM images of micropatterned HMA-co-HDDMA polymers

(A-C) SEM images are shown of a pattern with a 50  $\mu\text{m}$  periodicity and a channel amplitude of 8  $\mu\text{m}$ . (D-F) SEM images are shown of a pattern with a 10  $\mu\text{m}$  periodicity and a channel amplitude of 250 nm. Top-down view (A),(D); cross-sectional view (B),(E); angled cross-sectional view (C),(F). Note the gradual transitions between ridges and grooves.



generated and analyzed for maximum rate of propagation ( $R_p$ ), time to reach maximum rate and double bond conversion. The response surfaces will be used in conjunction with further work to understand reaction kinetic effects on microfeature formation during masked photopolymerization. Developing a model that relates polymerization reaction kinetics to controllable microfeatures would be a powerful tool and predictor for fabrication of contact guidance substrates for future cell-material interaction studies (Table 3).

### Max Rate of Propagation ( $R_p$ )

The max  $R_p$  was determined from DSC measurements using the equation shown in Figure 6.

The suggested special quartic model gave the best statistical fit for the Max  $R_p$  data with an F-value of 165.24. The measure of signal-to-noise ratio (Adeq Precision) is much greater than 4 (at 36.14), illustrating that the response in relation to the error is significant. The adjusted R-squared value for the special quartic model is 0.9835, indicating a strong fit.

The special quartic model equation developed for Max  $R_p$  is:

$$\text{Max } R_p = 2.919 \times 10^{-3} \mathbf{A} + 0.032 \mathbf{B} + 0.033 \mathbf{C} - 0.023 \mathbf{AB} - 0.037 \mathbf{AC} + 0.026 \mathbf{BC} - 1.27 \mathbf{A}^2 \mathbf{BC} + 0.71 \mathbf{AB}^2 \mathbf{C} + 1.04 \mathbf{ABC}^2$$

The highest values of polymerization rate are obtained using a fairly even ratio of HDDMA to HEMA and little if any HMA (Figure 7). It should be noted that HMA has very low max  $R_p$  values principally because it does not undergo

TABLE 3

Lattice points (1-10) and checkpoints (11-13) for tricomponent mixture experiments for DOE analysis and modeling

Lattice Points	HMA	HDDMA	HEMA
1	1	0	0
2	0	1	0
3	0	0	1
4	0.667	0.333	0
5	0.333	0.667	0
6	0	0.667	0.333
7	0	0.333	0.667
8	0.333	0	0.667
9	0.667	0	0.333
10	0.334	0.334	0.333
11	0.5	0.25	0.25
12	0.25	0.5	0.25
13	0.25	0.25	0.5

FIGURE 6

### Max Rate of Propagation - $R_p$

The max  $R_p$  was determined from DSC measurements using the following equation:

$$R_p = Q \left( \frac{M_1}{x_1 m_T n_1 \Delta H_{pol}} + \frac{M_2}{x_2 m_T n_2 \Delta H_{pol}} + \frac{M_3}{x_3 m_T n_3 \Delta H_{pol}} \right)$$

$R_p$  = rate of propagation ( $s^{-1}$ )

Q = heat released during polymerization (W)

$M_{1,2,3}$  = molecular weight of each monomer species (g/mol)

$x_{1,2,3}$  = fraction of sample mass for each monomer species

$m_T$  = total sample mass used in DSC measurements (g)

$n_{1,2,3}$  = number of double bonds available for polymerization on each monomer

$\Delta H_{pol}$  = enthalpy of polymerization (J/mol)\*

\*Heat of polymerization was assumed to be a general methacrylate value of 54.8 kJ/mol for each monomer species.<sup>14</sup> Maximum  $R_p$  was measured as a system response as it may play a crucial role in the development and control of micropattern fabrication using masked photopolymerization.

autoacceleration under the given conditions. Autoacceleration occurs in radical polymerization when system vitrification becomes high enough as to inhibit biradical termination, but low enough to allow monomer diffusion to propagating kinetic chains. As a consequence of inhibited termination reactions,  $R_p$  dramatically increases prior to its subsequent rapid decrease once propagation reactions become strongly inhibited by the viscosity of the system. Neat HDDMA increases quickly in viscosity and thus undergoes autoacceleration since it is a difunctional methacrylate and undergoes crosslinking. While HEMA is only a monofunctional methacrylate, the hydroxyl group on each monomer enables the system to

undergo pseudo-crosslinking with the continued formation and breaking of hydrogen bonds. Accordingly, it also undergoes a strong autoacceleration effect. The model appears to strongly fit the physical phenomenon observed through DSC experiments.

Based on the equation coefficients, the concentration of HDDMA and HEMA have a much more significant effect on Max  $R_p$  than does that of HMA. It should be noted that the complex quartic interaction terms have the largest coefficients, illustrating that response is not solely additive, but that the interactions between monomers in the prepolymer formulation are also significant.

#### Time to Max $R_p$

In addition to the actual max  $R_p$ , the time required to reach the max may also be relevant to generation and control of photopolymerized microfeatures. Accordingly, the time to max  $R_p$  was measured during each of the DSC experimental runs (Figure 8).

As with the model for max  $R_p$ , a special quartic model gave the best statistical fit for the given data with an F-value of 10.37. There is only a 0.01% chance that the model occurs due to noise. The measure of signal-to-noise ratio (Adeq Precision) is greater than 4 (at 12.42), illustrating that the response in relation to the error is significant. The adjusted R-squared value for the special quartic model is 0.773, indicating a relatively good fit, but not as strong as that seen for the max  $R_p$  model.

The special quartic model equation developed for time to max  $R_p$  is:

$$T_{\max R_p} (s) = 4.6A + 36.29B + 49.68C - 82.83AB - 127.02AC - 44.48BC + 5598.44A^2BC - 1769.61AB^2C - 1862.68ABC^2$$

DOE methodology is a particularly valuable tool to determine response directionality. Based on a relatively

low number of experiments, a “sweet spot” with defining contours can be determined for both long and short times to reach max  $R_p$ . Since HDDMA undergoes autoacceleration

most quickly due to its effects on viscosity as a crosslinker, the higher its concentration, the faster the mixture reaches its max  $R_p$ . HMA also reaches max  $R_p$  very quickly, but it should be

FIGURE 7

Tricomponent mixture response surface of max  $R_p$  for HMA-HDDMA-HEMA mixtures

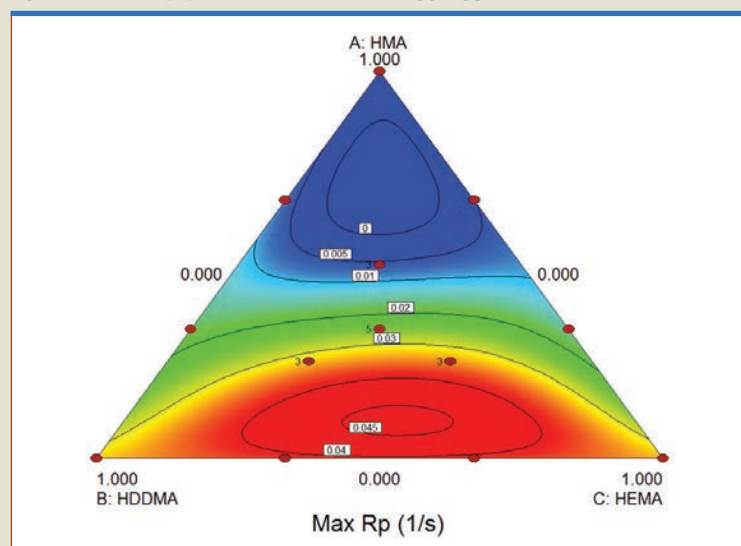
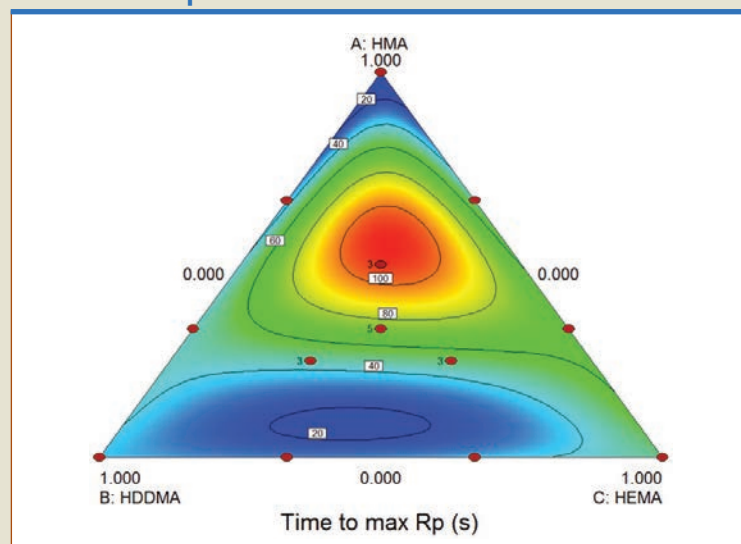


FIGURE 8

Tricomponent mixture response surface of time to reach max Rp for HMA-HDDMA-HEMA mixtures



noted that its max was on the order of 5-10 times lower than that seen for neat HDDMA and HEMA systems. HMA reaches max  $R_p$  very early on in the reaction and does not undergo the radical polymerization autoacceleration effect that would delay onset of the maximum propagation rate. Accordingly, max  $R_p$  takes longer to achieve with increasing concentrations of HMA until the system becomes sufficiently linear (i.e., lacking covalent HDDMA crosslinks or pseudo HEMA crosslinks) as to prevent auto-acceleration. Thus, a global maximum for this particular tricomponent mixture is observed near the 50 HMA, 25 HDDMA, 25 HEMA point used in the initial model generation.

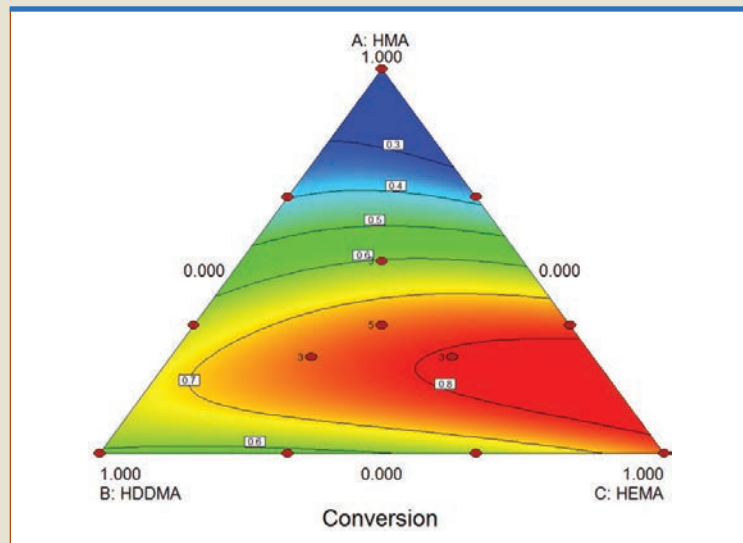
Based on the equation coefficients, the concentration of HDDMA and HEMA have a much more significant effect on time to max  $R_p$  than does that of HMA. It should be noted that the complex quartic interaction terms have, by far, the largest coefficients, thus illustrating that response is not solely additive, but that the interactions between monomers in the prepolymer formulation is also significant. In this case, the interaction terms so thoroughly dwarf the linear terms that they could be excluded if not for the hierarchy rule to generate the model.

#### **Methacrylate Double-Bond Conversion**

Conversion was determined by calculating the area under the  $R_p$  curve using the trapezoidal rule. It is assumed that conversion will also play a significant role in the observed feature dimensions generated through masked photopolymerization. Accordingly, its response for the DOE tricomponent response surface analysis was also measured (Figure 9). In contrast to the models suggested for max  $R_p$  and time to max  $R_p$ , a cubic model gave the best statistical fit for the given data with an F-value of 27.84.

## FIGURE 9

### Tricomponent mixture response surface of polymer conversion for HMA-HDDMA-HEMA mixture



The measure of signal-to-noise ratio (Adeq Precision) is greater than 4 (at 18.78), illustrating that the response in relation to the error is significant. The adjusted R-squared value for the special quartic model is 0.917, indicating a strong fit.

The cubic model equation developed for conversion is:

$$\text{Conversion} = 0.26\mathbf{A} + 0.59\mathbf{B} + 0.74\mathbf{C} + 0.43\mathbf{AB} + 0.31\mathbf{AC} - 0.28\mathbf{BC} + 4.57\mathbf{ABC} - 0.94\mathbf{AB(A-B)} - 1.58\mathbf{AC(A-C)}$$

Increasing HEMA concentration generally correlates with an increased final conversion of the given tricomponent system (Figure 9). It is likely that HDDMA cannot reach as high of a conversion as predominantly HEMA mixtures due to rapid vitrification caused by covalent crosslinks. In contrast, HEMA still undergoes a strong autoacceleration affect, but propagating species are not trapped as early in the reaction due to the transitory nature of the pseudo-crosslinks (i.e., hydrogen bonds) in the HEMA network. Double-bond

conversion is low for mixtures that are predominantly HMA in concentration.

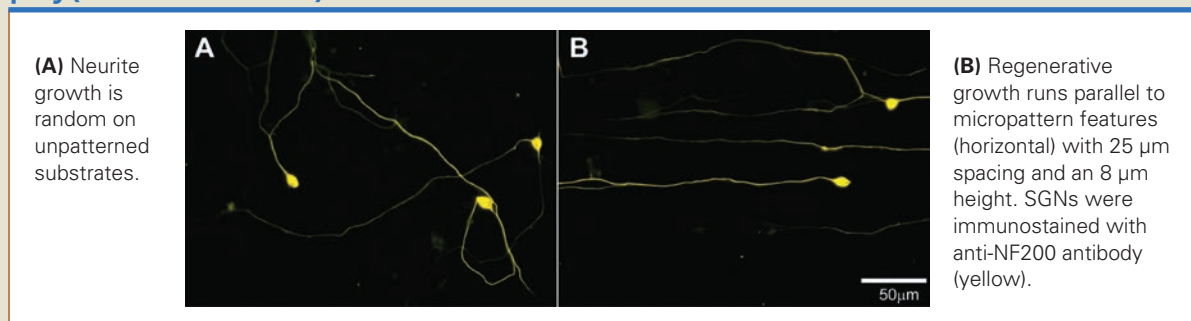
Based on the equation coefficients, the concentration of HDDMA and HEMA has a more significant effect on conversion than does that of HMA. However, the interaction factors, particularly that between all three monomer species (ABC), is the strongest contributing factor to the final conversion outcome. The equation again illustrates that the response is not solely additive, but that the interactions between monomers in the prepolymer formulation is very significant.

#### **Inner Ear Nerve Cells Orient to Surface Features**

Spiral ganglion neurons (SGNs), inner ear nerve cells, were cultured on 40/60 wt% poly(HMA-co-HDDMA) parallel line-space gratings and on unpatterned samples as a control. Neurites were visualized with an epifluorescent microscope and measured using Image J. Dissociated SGNs cultured on unpatterned substrates extended regenerating neurites in random

## FIGURE 10

### Dissociated SGN neurite growth on unpatterned or patterned 40/60 wt% poly(HMA-co-HDDMA)



directions across the polymer surface (Figure 10A). However, regenerating neurite outgrowth was strongly oriented in the direction of the microfeatures (horizontal) when SGNs were cultured on patterned substrates (Figure 10B). Additionally, neurites encountering the pattern at a steep angle relative to the features were caused to turn and follow the direction of the pattern after short distances. SGN neurites, therefore, respond and

orient to gradually sloping features formed by the described patterning photopolymerization method.

#### Tuning Extent of Neurite Alignment

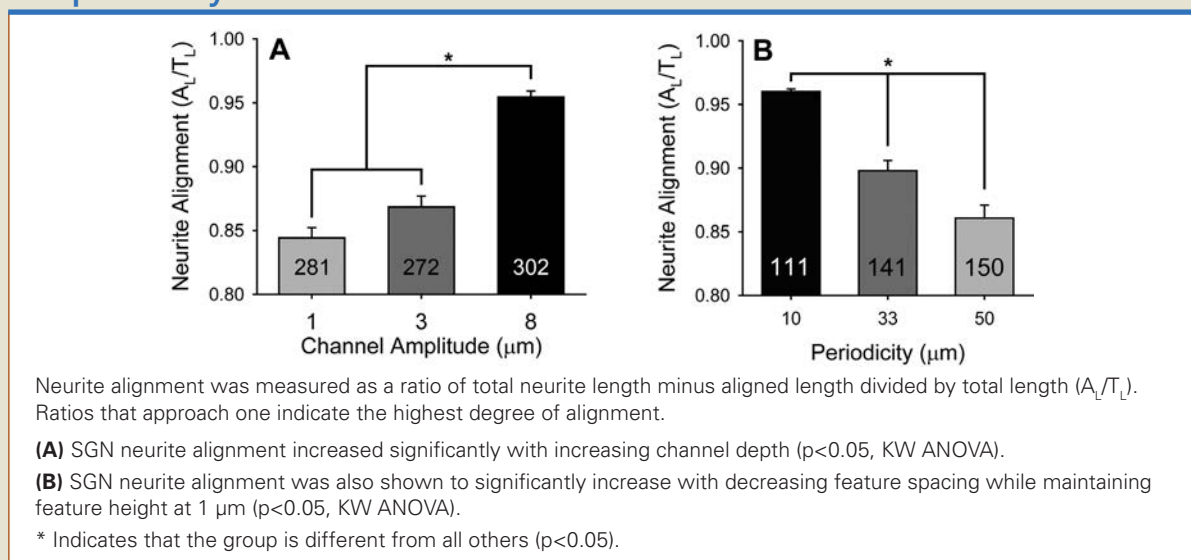
For line-space grating patterns, SGN neurite alignment was measured as the ratio of aligned distance per length of neurite ( $A_L/T_L$ ). The closer the ratio is to one, the more aligned the entire neurite is to the pattern features. To explore the effect of channel amplitude on SGN neurite orientation, pattern

pitch was kept constant at 50 μm and channel amplitude was varied from 1 to 8 μm by shuttering the UV radiation source at specific time steps during the reaction. The extent of SGN neurite orientation to feature height significantly increases with increasing channel depth (Figure 11A).

Feature frequency also significantly affected the total extent of directed neurite regeneration. Channel amplitude was maintained at 1 μm

## FIGURE 11

### SGN neurite alignment to line-space gratings depends on channel depth and periodicity



and cells were cultured on patterns with periodicities of 10, 33 and 50  $\mu\text{m}$ . SGN neurite alignment significantly increased with increasing feature frequency (Figure 11B). Interestingly, orientation on a 10  $\mu\text{m}$  periodicity 1  $\mu\text{m}$  amplitude sample was not statistically different from SGN neurite orientation on a 50  $\mu\text{m}$  periodicity and 8  $\mu\text{m}$  amplitude.

## Conclusion

The described research presents a radiation-curing method to generate physical micropatterns in biomaterials and demonstrates the first use of topographic cues to align neurites of neurons from the inner ear. It is anticipated that the results of this interdisciplinary effort will contribute significantly to polymer neural regeneration technology and will lead to novel clinical techniques to improve CIs and, consequently, the quality of life for CI patients. Further, the knowledge gained about peripheral nervous system growth on these engineered biomaterials may improve existing or future therapies to treat PNS damage and may also enhance other facets of tissue engineering. ▀

## Acknowledgements

The authors would like to acknowledge the National Center for Research Resources (grant number UL1RR024979), a part of the National Institutes of Health and the American Hearing Research Foundation, for project funding. We also acknowledge funding from the Department of Defense for a National Defense Science and Engineering Graduate research fellowship awarded to the presenting author.

## References

- O'Leary, S.J.; Richardson, R.R.; McDermott, H.J. Principles of design and biological approaches for improving the selectivity of cochlear implant electrodes. *Journal of Neural Engineering* 2009, 6, 055002.
- Leng, T.; Wu, P.; Mehenti, N.Z.; Bent, S.F.; Marmor, M.F.; Blumenkranz, M.S.; Fishman, H.A. Directed retinal nerve cell growth for use in a retinal prosthesis interface. *Invest. Ophthalmol. Vis. Sci.* 2004, 45, 4132-4137.
- Winter, J.O.; Cogan, S.F.; Rizzo, Joseph F., III Retinal prostheses: current challenges and future outlook. *Journal of Biomaterials Science-Polymer Edition* 2007, 18, 1031-1055.
- Shannon, R.V.; Fu, Q.J.; Galvin, J., 3rd The number of spectral channels required for speech recognition depends on the difficulty of the listening situation. *Acta Otolaryngol. Suppl.* 2004, (552), 50-54.
- Rubinstein, J.T. How cochlear implants encode speech. *Curr. Opin. Otolaryngol. Head Neck Surg.* 2004, 12, 444-8.
- Evans, A.J.; Thompson, B.C.; Wallace, G.G.; Millard, R.; O'Leary, S.J.; Clark, G.M.; Shepherd, R.K.; Richardson, R.T. Promoting neurite outgrowth from spiral ganglion neuron explants using polypyrrole/BDNF-coated electrodes. *Journal of Biomedical Materials Research Part A* 2009, 91A, 241-250.
- Brors, D.; Aletsee, C.; Schwager, K.; Mlynski, R.; Hansen, S.; Schäfers, M.; Ryan, A.F.; Dazert, S. Interaction of spiral ganglion neuron processes with alloplastic materials in vitro. *Hear. Res.* 2002, 167, 110-121.
- Mehenti, N.Z.; Peterman, M.C.; Leng, T.; Marmor, M.F.; Blumenkranz, M.S.; Bent, S.F. A retinal interface based on neurite micropatterning for single-cell stimulation. *Invest. Ophthalmol. Vis. Sci.* 2003, 44, U704-U704.
- Roehm, P.C.; Hansen, M.R. Strategies to preserve or regenerate spiral ganglion neurons. *Curr. Opin. Otolaryngol. Head Neck Surg.* 2005, 13, 294-300.
- Guenther, E.; Troger, B.; Schlosshauer, B.; Zrenner, E. Long-term survival of retinal cell cultures on retinal implant materials. *Vision Res.* 1999, 39, 3988-3994.
- Cui, X.Y.; Wiler, J.; Dzaman, M.; Altschuler, R.A.; Martin, D.C. In vivo studies of polypyrrole/peptide coated neural probes. *Biomaterials* 2003, 24, 777-787.
- Tuft, B.W.; Li, S.; Xu, L.; Clarke, J.C.; White, S.P.; Guymon, B.A.; Perez, K.X.; Hansen, M.R.; Guymon, C.A. Photopolymerized microfeatures for directed spiral ganglion neurite and Schwann cell growth. *Biomaterials* 2013, 34, 42-54.
- Clarke, J.C.; Tuft, B.W.; Clinger, J.D.; Levine, R.; Figueroa, L.S.; Allan Guymon, C.; Hansen, M.R. Micropatterned methacrylate polymers direct spiral ganglion neurite and Schwann cell growth. *Hear. Res.* 2011, 278, 96-105.
- Lee, H.; Colby, C. Heat of polymerization of nine mono-, di-, and trimethacrylate esters tested neat and with low levels of peroxide by dynamic differential scanning calorimetry. *Dental Materials* 1986, 2, 175-178.

—Bradley W. Tuft was a National Defense Science and Engineering Graduate Research Fellow in chemical engineering (now a senior product development engineer at Dow Corning); Linjing Xu is a research associate; Austin Hangartner is an undergraduate research assistant; Scott White was an undergraduate research assistant; and Allan Guymon is the department chair at the University of Iowa, Department of Chemical and Biochemical Engineering, Iowa City, Iowa. Marlan Hansen is a professor of Otolaryngology at the University of Iowa Hospitals and Clinics, Department of Otolaryngology, Iowa City, Iowa.